Precision Needle Tip Localization using
Optical Coherence Tomography Images for Subretinal Injection

Mingchuan Zhou[1], Kai Huang[2], Abouzar Eslami[3], Hessam Roodaki[1],
Daniel Zapp[4], Mathias Maier[4], Chris P. Lohmann[4], Alois Knoll[1] and M. Ali Nasseri[4]

Abstract—Subretinal injection is a delicate and complex microsurgery, which requires surgeons to inject the therapeutic substance in a pre-operatively defined and intra-operatively updated subretinal target area. Due to the lack of subretinal visual feedback, it is hard to sense the insertion depth during the procedure, thus affecting the results of surgical outcome and hindering the widespread use of this treatment. This paper presents a novel approach to estimate the 3D position of the needle under the retina using the information from microscope-integrated Intraoperative Optical Coherence Tomography (iOCT). We evaluated our approach on both tissue phantom and ex-vivo porcine eyes. Evaluation results show that the average error in distance measurement is 4.7 μm (maximum of 16.5 μm). We furthermore, verified the feasibility of the proposed method to track the insertion depth of needle in robot-assisted subretinal injection.

I. INTRODUCTION

Subretinal injection is a form of vitreoretinal surgery. For this operation, conventionally, the surgeon is required to inject a microcannula into a specific area of the translucent retina to a certain depth, this is a target which is normally defined pre-operatively (see Fig. 1). The precise control of the depth of the needle tip is critical for subretinal injection, as a shallow injection will not release sufficient drug and an overly deep injection may result in irreparable damage to the retinal pigment epithelium (RPE) and causing vessel rupture. On the other hand, this critical depth control will be affected by hand tremor of the surgeon and visual artifacts caused by the microscopic view of the target area. Therefore, subretinal injection is known to be a delicate and complex procedure, which needs enhanced skills and considerations.

To overcome surgeon's hand tremor, many researchers in the recent years have introduced high precision robotic setups in different scales and design mechanisms [1]–[10]. Over years, these ophthalmic robots are becoming mature to enter the clinical trial, for instance Robotic Retinal Dissection Device (R2D2) performed the world first robotic Internal Limiting Membrane (ILM) peeling surgery [11], [12]. Although robots proved their abilities to suppress the

[1]Department of Computer Science, Technische Universität München, Germany. {zhoum;hessam.roodaki;knoll}@in.tum.de.
[2]Key Laboratory of Machine Intelligence and Advanced Computing, School of Data and Computer Science, Sun Yat-sen University, China. huangk36@mail.sysu.edu.cn
[3]Carl Zeiss Meditec, Germany. abouzar.eslami@zeiss.com
[4]Department of Ophthalmology, Klinikum rechts der Isar, Technische Universität München, Germany.
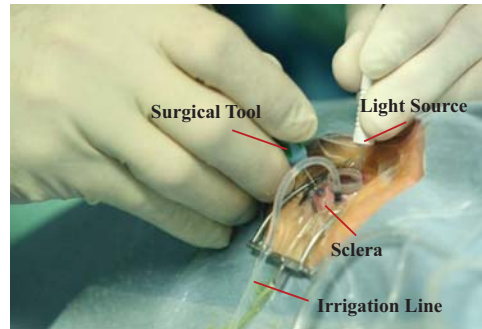{daniel.zapp;athias.maier;chris.lohmann;
ali.nasseri}@mri.tum.de

Fig. 1. A conventional subretinal injection setup. The incision ports are made by trocars at the sclera in a circle 3.5mm away from the limbus to provide entrance for surgical tools: light source, instrument, and irrigation line [1]. The light source is used to illuminate the intended area on the retina, allowing its planar view to be analyzed by surgeon through the ophthalmic microscope. The irrigation line is used for liquid injection to maintain appropriate intraocular pressure.

hand tremor from surgeons, the challenge of the intra-retinal needle localization still remains. The reason is multi-fold. First is the lack of proper visual feedback, specifically it is hard to sense the needle-tip depth through a conventional microscopic (en-face) view during the insertion of the needle into the translucent retinal layers. Secondly, the information from only the kinematics of the robot is not sufficient to accurately estimate the needle tip position because of the very thin, long, and flexible needle body [13]. Last but not the least, 3D ultrasound and MRI imaging modalities, which typically are used in non-microsurgical scenarios, do not have enough precision to be directly applied to subretinal interventions. These imaging modalities normally offer needle localization error of around 500 μm [14], while the average thickness of retina is around 250 μm [15] which requires a maximum error of 25 μm for needle localization. A promising ophthalmic imaging modality is Optical Coherence Tomography (OCT). OCT is originally used for ophthalmic diagnosis and it is known for having suitable resolution with non-invasive radiation that brings minimum risk of toxicating the ocular tissue. The latest OCT machines has been developed to even give realtime information of the microstructural anatomies and the interactions between surgical instrument and intraocular tissues [16].

Currently there are two methods to intraoperatively deploy OCT data for intra-ocular needle localization. The first method proposed by Cheon et al. [17] is to detect the distance of the target surface from the OCT probe using

A-scans. Afterwards, the insertion depth can be calculated considering the distance of the needle tip and OCT probe is known. The limitation of this method is that the needle tip needs to be perpendicular to the target surface. Furthermore, the integration of OCT probe into the needle makes the instrument more complicated in process and maintenance. Instead of integrating OCT probe in surgical instrument, the microscope-integrated intraoperative OCT, which share the same path with microscope to capture volumetric images, is used to estimate the needle tip position. The benefit of this method is to avoid using modified needles but utilizing conventional subretinal cannulas. Due to the optical property of the metallic instruments, the needle above the retina can have a clear upper surface and a shadow on the retina in B-scan, as shown in Fig. 2(a). Making use of this feature, Roodaki et al. [18] estimated the distance between surgical tool tip and the underlying tissue. However, when the needle tip is inside the retina, it is hard to reliably distinguish it from the retina because of having similar intensity and unclear shadow, an example of which is shown in Fig. 2(b). Therefore, it is difficult to estimate the position and orientation of the needle tip when it is inside the retina.

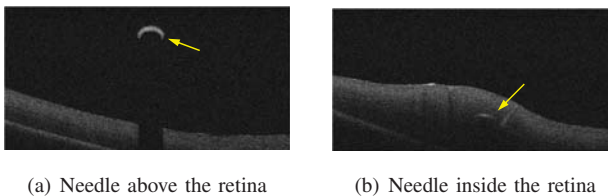(a) Needle above the retina   (b) Needle inside the retina

Fig. 2.   The needle fragment and retina in OCT B-scan images. Needle fragment is labeled by arrow.

To address this issue, this work proposes a novel approach to localize the needle tip within the retinal surface using 3D OCT images. The main premise of this paper is that the needle tip distortion during the insertion is ignored, due to the fact that the interaction force between retinal tissue and the surgical tool is normally below 15 mN [19]. With this assumption, our approach consists of needle and retinal surface reconstruction, Computer Aided Design (CAD) model based calibration, and distance measurement of a needle tip to retinal surface. To precisely model the shape of the needle which is inserted inside the eye, CAD model of the needle is reconstructed and registered to 3D point cloud of the needle obtained from the OCT images when it is still above the retina. Afterwards, the needle tip is predicted following its insertion into the retina. The distance of the needle tip to retina is computed and the retinal surface is also reconstructed to give a better perception for the surgeon. Our approach is evaluated on both tissue phantom and ex-vivo porcine eyes. Evaluation results show that the maximum error in distance measurement of needle tip to retinal surface is within 16.5 µm, and this error achieves the clinical tolerance for subretinal injection. We also verified the feasibility of our proposed method to control the insertion depth in robot-assisted subretinal injection.

The rest of this paper is organized as follows. Section II briefly describes the related work. The background information is presented in Section III. Section IV details the method. Section V gives the accuracy performance of proposed method and verifies the concept of insertion depth measurement with iRAM!S eye surgical robot [9]. Section VI concludes this paper with the discussion and the presentation of future work.

II. RELATED WORK

Needle localization have been intensively researched in various 3D medical imaging technologies, e.g. CT scans, fluoroscopy, MRI or ultrasound. However, these imaging technologies can hardly achieve the ideal resolution for subretinal injection. As an example, for MRI-guided interventions with millimeter resolution in breast and prostate biopsies, 18G (Ø=1.27 mm) needle is used, while for subretinal injection, 32G (Ø=0.235 mm) needle requires resolution of submillimeter [20]. Moreover, due to the needle fragments in OCT images it contains more geometrical information which determines the accuracy of needle localization and consequently the localization method for other 3D imaging technologies can not be directly used in OCT images.

Despite the importance of the application, little work has been done for needle localization in OCT images. Some researchers deployed OCT probe on the instrument for distance estimation between the surgical tool and eye tissue. Song et al. [8] developed a robotic surgical tool with an integrated OCT probe to estimate single dimensional distance between surgical tool and eye tissue for membrane peeling purposes. Yu et al. [21], and Liu et al. [22] deployed OCT probe to assist robotic ophthalmic surgery. They focused on integrating the OCT probe on the ophthalmic microforceps. Their method ensures the instruments constantly keeps its safe distance from the retina. To estimate the needle insertion depth into the retina, Cheon et al. [17] developed a depth-locking handheld instrument which can control the insertion depth with OCT sensing. The integration of OCT probe into the instrument can simplify the acquisition setup avoiding the necessity of imaging through the cornea and crystalline lens. However, it makes the instrument more complicated in process and maintenance. Moreover, the mechanism of the proposed method need a perpendicular direction of insertion with respect to the target surface which may restrict the flexibility of the operation.

The microscope-integrated OCT shares the same optical path with microscope which has been used in ophthalmic operating theater and proved having a positive impact on the surgical outcome [16]. With such an imaging principle, OCT images are captured without modification of instruments, which is obviously easier to apply in the current operating theaters and surgical workflows. Roodaki et al. [18] estimated the distance between surgical tool and the underlying tissue using geometrical information of instrument. This method is designed for those vitreoretinal operations that the instrument is operating above the retina (e.g. ILM peeling). In order to overcome the challenges of estimating the insertion depth for
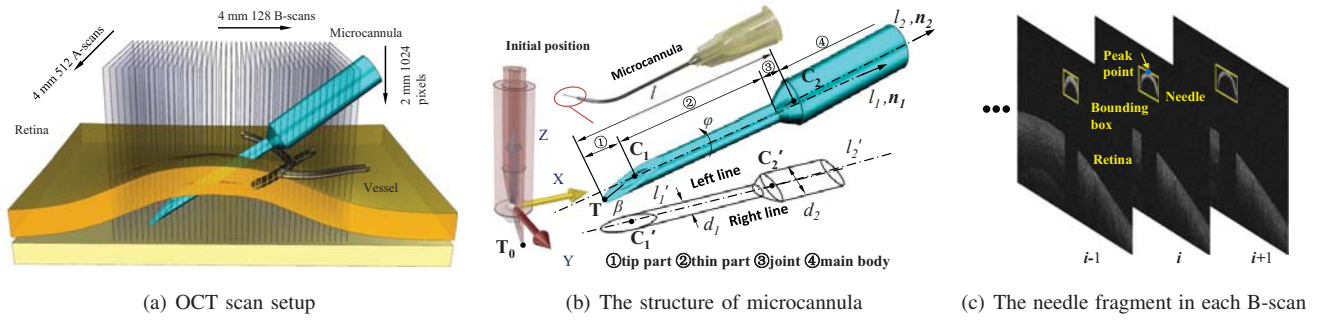
| (a) OCT scan setup | (b) The structure of microcannula | (c) The needle fragment in each B-scan |

Fig. 3. (a): OCT scan setup for subretinal injection. OCT scans a cube with a resolution of 128×512×1024 pixels in 4 mm× 4 mm × 2 mm. (b): The structure of the microcannula and its projection. The pose and position of the microcannula in space can be represented by the space transformation of CAD models from initial position. (c): The needle points are enveloped by a bounding box in each B-scan image.

subretinal injection, this paper propose a precision needle tip localization method using 3D OCT images. The microscope-integrated OCT is adopted to capture the information thus without modification of conventional instruments.

III. BACKGROUND

This section introduces the background of the proposed framework which includes the OCT image acquisition, the geometrical structure of a commercially available microcannule for subretinal injection and the image preprocessing.

A. OCT Image Acquisition

Our setup contains an OPMI LUMERA 700 with integrated RESCAN 700 intraoperative OCT engine, and *CALLISTO* eye assistance computer system (Carl Zeiss Meditec AG.). The *CALLISTO* eye assistance computer system is utilized to display the microscopic image and two cross OCT images at the same time, and a foot panel is connected to the system for helping to relocate the OCT scan area. All the images are acquired on a tissue phantom and during ex-vivo experiments with porcine eyes using conventional subretinal cannulas. The soft cheese is used as a simple tissue phantom because it has the similar OCT imaging result as ocular tissues and it is readily available. In order to acquire sufficient visual information for needle reconstruction and calibration, we reprogrammed the original iOCT device and the movement of its internal mirror galvanometers to obtain the highest resolution with 128 B-scans, each with 512 A-scans (4 mm×4 mm) [23]. Each A-scan has 1024 pixels for 2 mm depth information in tissue, see Fig. 3(a).

B. Geometrical Structure of the Needle

The conventional microcannula used for subretinal surgery is shown in Fig. 3(b). The microcannula is characterized to four parts: the tip part, the thin part, the joint and the main body. Its parameters consist of 20G (Ø=0.908 mm) main body, 32G (Ø=0.235mm) thin part with length of 3 mm and 15° beveled angle (Eagle Labs Inc.). The thin part and the main body are considered as the shape of a cylinder. The tip part and the thin part are represented by the bevel center point C_1, space vector n_1, diameter d_1, and bevel angle β. The main body is represented by body start point C_2, space vector

n_2 and diameter d_2. Assume l_1 and l_2 are the axis of thin part and the center axis of the main body respectively, and l_1' and l_2' are their corresponding projection on XOY plane. C_1' and C_2' are the projection of C_1 and C_2, respectively. The left line and right line are the borderline of the thin part projection on XOY plane. The pose and position of microcannula in space can be represented by a CAD model, see Fig. 3(b).

Due to the manufacturing defects and unexpected forces causing deformations during needle transportation and sterilization, we cannot precisely model the needle according to the specifications provided by the manufacturer. For example, we cannot simply assume that the vectors n_1 and n_2 are the same. Only a 5 degree difference between these vectors can cause an error of 250 μm in the measurement of the tip. Hence, the parameters for the thin part and the main body need to be represented separately and calibrated to achieve the desired precision for ophthalmic surgery. Following the proper needle calibration, the tip of microcannula T is determined by transforming CAD models (see Fig. 3(b) translucent CAD models) from the initial needle tip position T_0. In the inial position, C_1 and C_2 are at the origin point of coordinate system, meanwhile l_1 and l_2 are coincide with z axis. Therefore, we can calculate T_0 as follows,

$$\mathbf{T_0} = (\frac{d_1}{2}, 0, \frac{d_1}{2\tan(\beta)}) \tag{1}$$

C. OCT Image Preprocessing

The main goal of the image preprocessing is to segment the needle fragment from tissue in each B-scan image. Based on the needle shadow principle from our previous work [24], [25], the needle and retinal surface can be segmented with dissolution of noise influence in each B-scan image when the needle is still above the retina. The position of the needle points can be calculated from the index of OCT B-scan and pixels position in current OCT B-scan image. See Fig. 3(c), in every B-scan, the needle points can be enveloped by the bounding box $\mathbf{B}_i = (Bx_i, By_i, Bz_i, w_i, h_i)$, $(i = 1, ..., n)$ where (Bx_i, By_i, Bz_i) is the position of the top left corner of bounding box, w_i and h_i are the width and height of the box respectively, and n is the total number of bounding boxes.
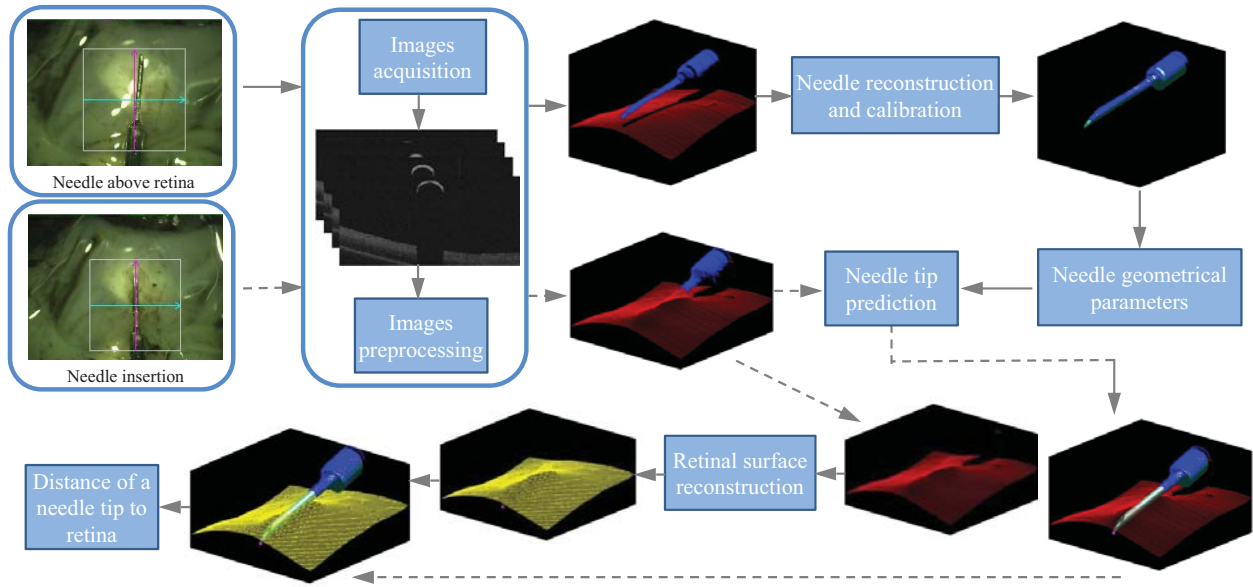
4035

Fig. 4. The framework of the method.

IV. METHOD

In this section, we present our approach, an overview of which is depicted in Fig. 4. Based on the OCT image preprocessing mentioned in the previous section, the needle point cloud and retinal surface point cloud can be segmented before the needle injects into the retina. The point cloud of the needle is then classified into four parts corresponding to the structure of microcannula. With these parts of point cloud, the needle CAD model is calibrated preciously with its geometrical parameters when the needle is above the retina. During the needle insertion, the CAD model of the needle is registered to the needle point cloud which remains above the surface. The tip of the needle is predicted using geometrical space transformation from its initial position. Simultaneously, the retinal surface is reconstructed to give the surgeon or the automatic system a better perception and finally the distance between the needle tip and the retinal surface is calculated for surgical reference. In the following, details of different components are discussed.

A. Needle Reconstruction and Calibration

Needle reconstruction and calibration is designed and processed when the needle is above the retina. The main geometrical parameters of needle are calculated to correct the needle CAD model for high precision intention. With the OCT image preprocessing, we can calculate the position of the needle and the surface points together with corresponding bounding box Bx_i. The variation of w_i with Bx_i reflects the geometrical information of the microcannula, where w_i increases along the tip and the joint, and remains constant along the thin part and the main body. Hence, $\mathbf{B}_i$ is divided in four segments with three break points. The bounding boxes are filtered as outliers if they have a large deviation in peak point position or w_i. Thereafter, piecewise linear regression

with least square fitting is applied to find the break points as follows,

$$f(i) = \begin{cases} k_1 Bx_i + c_1, i \in [1,o] \\ c_2, i \in (o,p]; \\ k_2 Bx_i + c_3, i \in (p,q] \\ c_4, i \in (q,n] \end{cases} \qquad (2)$$

$$\{\bar{o},\bar{p},\bar{q}\} = \underset{o,p,q}{argmin} \frac{1}{n} \sum_{i=1}^{n} (f(i) - w_i)^2 \qquad (3)$$

Eq. 2 gives the shape pattern of the needle projection, where k_1, k_2, c_1, c_2, c_3, and c_4 are the parameters after fitting and o, p, and q are the indices to divide the points into groups. Eq. 3 minimizes the algebraic distance between w_i and corresponding fitting value $f(i)$, and gives the optimal indices $\bar{o}$, $\bar{p}$ and $\bar{q}$. Subsequently, break points can be calculated from solving the equations from adjacent lines.

The points in group of indices $i \in (\bar{q},\bar{n}]$ enveloped by the bounding box in each B-scan can be fitted by an ellipse. Through the ellipse center points, l_2 can be obtained with RANSAC fitting with equation $\frac{x-x_0}{n_x} = \frac{y-y_0}{n_y} = \frac{z-z_0}{n_z}$, where (x_0,y_0,z_0) is a point on l_2. The error threshold for RANSAC that defines the maximum deviation is set as 0.05 mm. Assuming the equation of l_2': $y = k_0 x + b_0$, the left side line and right side line for the edges of the main body can be represented as $y = k_0 x + b_1$ and $y = k_0 x + 2b_0 - b_1$, respectively. Both two lines are obtained by fitting data sets (Bx_i, By_i) and $(Bx_i, By_i + w_i)$, $i \in (\bar{p},\bar{q}]$ respectively. The diameter of the main part d_2 is calculated by the distance between the left and right lines.

Introducing the breakpoints into l_2', we obtain point $\mathbf{D_2'}$ $(d_{2x},d_{2y},0)$, see Fig. 5(a). $\mathbf{C_2'}$ has a certain shift to $\mathbf{D_2'}$ that is decided by the slope of l_2'. We can calculate the three parameters to represent the main body part as,

4036

$$\begin{cases} \mathbf{n}_1 = (n_x, n_y, n_z) \\ d_1 = \dfrac{2|b_1 - b_0|}{\sqrt{1 + k_0^2}} \\ \mathbf{C}_1 = (d_{2x} - \triangle x, d_{2y} - \triangle y, \dfrac{n_z}{n_x}(d_{2x} - \triangle x - x_0)) \end{cases} \quad (4)$$

where $\triangle x = \sqrt{\dfrac{k_0^2 d_2^2}{4(1 + k_0^2)}}$ and $\triangle y = \sqrt{\dfrac{k_0^4 d_2^2}{4(1 + k_0^2)}}$ are the shift distance from $\mathbf{D}_2'$ to $\mathbf{C}_2'$ in X and Y axis, respectively.

Similarly, we obtain l_1, $\mathbf{n}_1$, and d_1 which determine the pose of the thin part. Due to the fact that the needle bevel is upwards, we can reconstruct the needle tip part with the intersection of the bevel plane and thin part. The bevel plane is estimated by the RANSAC plane fitting [26] with the point cloud of tip part, see Fig. 5(a). The error threshold for RANSAC plane fitting that defines the maximum deviation is set as 0.01 mm. The bevel center point $\mathbf{C}_1$ can be calculated as the intersection point of the bevel plane Γ and the l_1. The tip part rotation φ and bevel angel β can be calculated as,

$$\begin{cases} \varphi = \arcsin(||\mathbf{n}_\Gamma \times \hat{\mathbf{n}}_\mathbf{z}||) \\ \beta = \arccos(||\mathbf{n}_\Gamma \times \mathbf{n}_1||) - \dfrac{\pi}{2} \end{cases} \quad (5)$$

where $\mathbf{n}_\Gamma$ is the unit normal of Γ in positive z direction and $\hat{\mathbf{n}}_\mathbf{z}$ is the unit normal in positive z direction. The length of the thin part l is calculated by the distance between point $\mathbf{C}_2$ and $\mathbf{T}$.
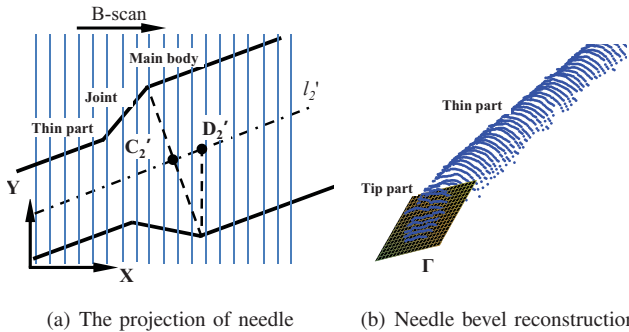
(a) The projection of needle   (b) Needle bevel reconstruction

Fig. 5. The diagram for the calculation of C_2' in XOY plane (a) and the needle bevel reconstruction (b).

B. Needle Tip Prediction

Based on aforementioned progress, the structure of the microcannula can be determined. Moreover, these configurations are used to calibrate and reconstruct the needle CAD model, see Fig. 6. When the needle is above the retina, the needle-tip $\mathbf{T}$ can be calculated by geometrical space transformation of needle-tip $\mathbf{T}_0$ from initial position.

$$\mathbf{T} = \mathbf{T}_0 R_z(\varphi) R(\hat{\mathbf{n}}_\mathbf{z}, \mathbf{n}_1) T(\mathbf{C}_1) \quad (6)$$

where R_z is the rotation matrix around Z axis with angle φ, $R(\hat{\mathbf{n}}_\mathbf{z}, \mathbf{n}_1)$ is the rotation matrix from $\hat{\mathbf{n}}_\mathbf{z}$ to $\mathbf{n}_1$, $T(\mathbf{C}_1)$ is the translation matrix.

(a) Microscopic en face view   (b) OCT en face view
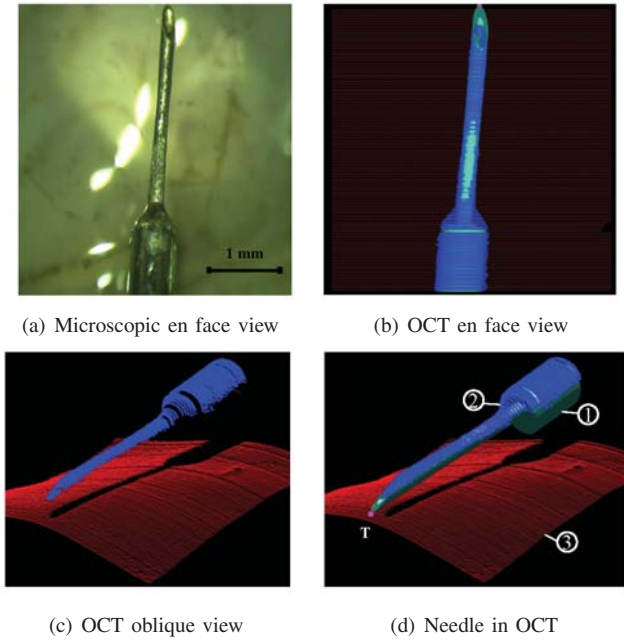
(c) OCT oblique view   (d) Needle in OCT

Fig. 6. The result of needle reconstruction and calibration. The needle in microscopic en face view (a) and the reconstructed and calibrated needle CAD model in OCT en-face view (b) are presented. The oblique view of OCT point cloud (c) and needle tip $\mathbf{T}$ prediction (marked by magenta piont) shown in (d) can give more information to guide the operation. ① represents CAD model of needle, ② represents the needle points cloud, and ③ presents the retinal surface points cloud.

During the injection, the tip part will be inside the tissue but the main body will still remain above the retina. In this situation, $\mathbf{C}_2$ and $\mathbf{n}_2$ are used to estimate the position and pose of the calibrated needle CAD model, see Fig. 7(a) and 7(b). The renewed position of the needle tip $\mathbf{T}^*$ can be updated by,

$$\mathbf{T}^* = \mathbf{T}R(\mathbf{n}_2, \mathbf{n}_2^*) T(\mathbf{C}_2^* - \mathbf{C}_2) \quad (7)$$

where $\mathbf{n}_2^*$ and $\mathbf{C}_2^*$ are the corresponding updated value for $\mathbf{n}_2$ and $\mathbf{C}_2$. $R(\mathbf{n}_2, \mathbf{n}_2^*)$ is the rotation matrix from $\mathbf{n}_2$ to $\mathbf{n}_2^*$. $T(\mathbf{C}_2^* - \mathbf{C}_2)$ is the translation matrix.

C. Retinal Surface Reconstruction and Distance of the Needle Tip to Surface

The retinal point cloud is sampled uniformly along XY grid by a factor decided by considering surface quality and processing time. The outliers in the point cloud are filtered by a statistical technique used in [27]. To approximate the missing points, which are lost due to the needle shadow and outliers, natural neighbor interpolation method is used.

The surface reconstruction is performed by a similar method used by Hoppe et al [28]. Given a set of points $\mathbf{X} = \{\mathbf{x}_1, \cdots, \mathbf{x}_n\}$ representing a surface M, a tangent plane is associated with each point $\mathbf{x}_i$, represented by a center $\mathbf{o}_i$ and a unit normal $\hat{\mathbf{n}}_i$. A neighborhood $Nbhd(\mathbf{x}_i)$ is defined using k points in $\mathbf{X}$ nearest to $\mathbf{x}_i$, where $\mathbf{o}_i$ and $\hat{\mathbf{n}}_i$ are calculated as the centroid, and the unit eigenvector associated with the lowest eigenvalue in the covariance matrix of $Nbhd(\mathbf{x}_i)$ respectively. Here, $k=20$ is used for the estimation of tangent

4037

plane. Then, a signed function d is defined to estimate the distance between a point $\mathbf{p}$ and the surface M as,

$$d(\mathbf{p}) = (\mathbf{p} - \mathbf{o_i}) \cdot \hat{\mathbf{n}}_{\mathbf{i}} \qquad (8)$$

The zero set of d will be the estimate of the surface. The extraction the iso-surface is done by the contouring algorithm, marching cubes [29]. The reconstructed retinal grid and the needle inside retina are shown in Fig. 7(c).

The distance of needle tip $\mathbf{T}$ from the retinal surface in z-axis can be calculated using d with modified parameters,

$$d(\mathbf{T}) = (\mathbf{T} - \mathbf{o_i^{XOY}}) \cdot \hat{\mathbf{n}}_{\mathbf{z}} \qquad (9)$$

where center $\mathbf{o_i^{XOY}}$ is calculated using k nearest points to $\mathbf{T}$ in the projection of *XOY* plane.
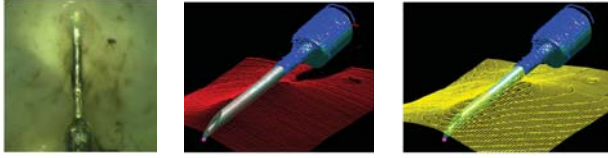
(a) Microscopic en-face view (b) Before retinal surface reconstruction (c) Retinal surface reconstruction

Fig. 7.   The needle is injected inside retina in microscopic image (a). Oblique view of the point cloud for OCT cube (b). Needle tip prediction based on CAD model and reconstructed retinal surface (c).

V. EXPERIMENTS AND RESULTS

Our experimental setup is depicted in Fig. 8. The iRAM!S eye surgical robot is mounted on an adjustment bracket and the motion of robot is controlled by the robot controller. The OPMI LUMERA 700 with integrated RESCAN 700 intraoperative OCT engine is fixed on the optical table to reduce the influence of ambient vibration. The foot panel is used to relocate the OCT scan area. The OCT is set to operate with the maximum available scanning speed (27000 A-scans per second), in cube resolution of $128 \times 512 \times 1024$ pixels. The implementation of our approach is executed on the *CALLISTO* eye assistance computer system with an Intel
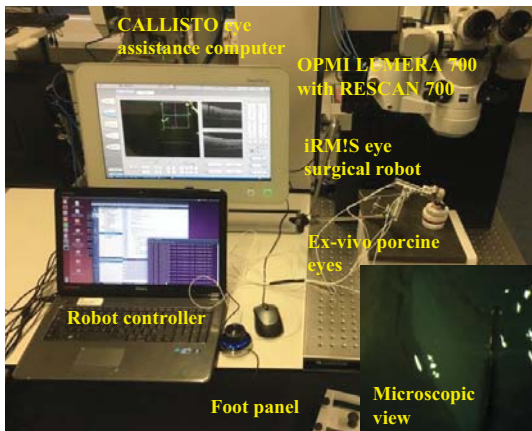

Fig. 8.   The experimental setup.

TABLE I

DESCRIPTIVE STATISTICS FOR THREE INTRINSIC DIMENSIONS (IN MICRON).

	Mean	Actual	AE	ME	RSME	0.95CI
d_1	234.0	230.0	4.0	6.8	4.2	[231.5-236.4]
d_2	671.8	670	1.7	5.7	3.0	[666.5-675.6]
l	3204.6	3200	4.6	45.7	21.5	[3152.4-3239.4]
$\bar{d_1}^5$	234.1	230.0	4.1	5.2	4.1	[233.1-234.9]
$\bar{d_2}^5$	671.6	670	1.6	4.7	1.8	[670.1-673.1]
$\bar{l}^5$	3204.8	3200	4.8	21.2	7.7	[3190.3-3216.1]

Core i7 CPU and a NVIDIA GeForce GTX 980i GPU with average speed of 0.4 s for each cube with parallel programming. We performed two types of experiments: 1) test-retest reliability and accuracy performance of proposed method, and 2) insertion depth tracking with the robot. Both experiments are conducted with both tissue phantom and cadaver porcine eyes.

A. Test-retest Reliability and Accuracy Performance

In this section, we conducted test-retest reliability experiments to verify the reconstruction and calibration results, and the accuracy performance of retinal surface to needle tip distance measurement using a manual micromanipulator. We estimate the variation of measurements referring to the intrinsic dimensions, the diameter of the thin part d_1, the length of the thin part l, and the diameter of the main body d_2. The actual values for these parameters are obtained by a digital caliper with a resolution of 10 μm after 10 times averaging of repeated measurements. We capture 80 image cubes with various injection postures above the retinal surface in ex-vivo porcine eyes.

We randomly select 5 estimated values and average these values from each dimension for 80 times to obtain $\bar{d_1}^5$, $\bar{d_2}^5$ and $\bar{l}^5$, respectively. Several statistical metrics are used to evaluate deviation of these measurements shown in Tab. I including: the average error of estimated value to the ground truth (AE), the error of maximum estimated value and actual value (ME), the root mean square error (RSME), and the 95% of estimated confidence interval (0.95CI). All the mean errors are within 5 μm which indicate that the proposed method has the capability to achieve accurate reconstruction and calibration results. Due to the fact that the needle is placed along the B-scan direction with scan resolution of 31.3 μm and the number of tip part points is relatively less than the thin part and main body part, l_1 has a relatively larger maximum error and RSME than the other two parameters. This could be improved by averaging parameters with several OCT cubes to achieve a higher accuracy. The 0.95CI for $\bar{l}^5$ can be significantly narrowed down compared to single evaluation of l.

The accuracy of the distance between retinal surface and the needle tip is tested with a 3-axes HS-6 manual micromanipulator (Märzhäuser Wetzlar GmbH) with 5 μm resolution on both tissue phantom and ex-vivo porcine eyes. The needle is fixed on a micromanipulator and the micromanipulator
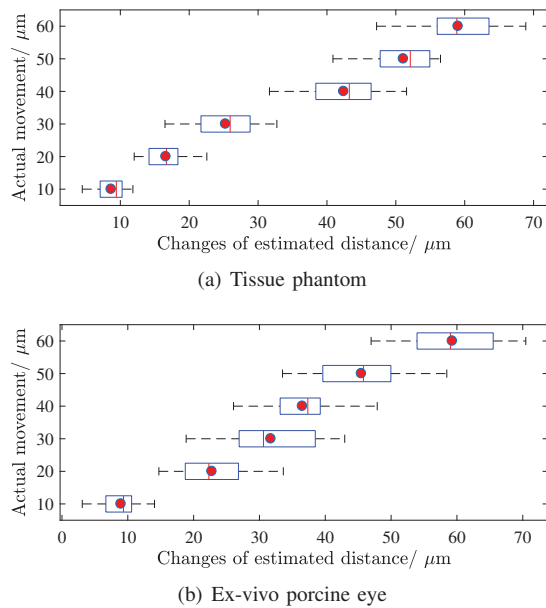
(a) Tissue phantom

(b) Ex-vivo porcine eye

Fig. 9. The actual movement of the needle that is mounted on a micromanuipulator and the change of estimated distance for the needle tip obtained from OCT cube. The whiskers show the minimum and maximum recorded change of the distance while the first and third quartile show the start and the end of the box. Band and red dot represent median and mean of the recorded changes respectively.

is fixed under the microscope on the optical table. The needle tip is moved up and down to change the distance of needle tip to the retinal surface. Before the movements, five OCT cubes are captured to calibrate and reconstruct the needle. Afterwards, in total 16 measurements are captured and modeled to predict needle tip for each movement. The results are presented in Fig. 9.

From the figures, one can find following observations: Firstly, the maximal error for all measurements is 16.5 μm and the maximal error for the mean estimated distance is 4.7 μm. The 0.95CI for overall movement error is [-11.9, 9.0] and [-14.0, 10.9] for tissue phantom and ex-vivo porcine eye, respectively. Secondly, the results of the estimated distance vary due to the vibration from the environment but the mean estimated distance value is consistent with the actual input movement. Thirdly, the variance of distance measurement with the porcine eyes are larger than with tissue phantom. This is likely due to the fact that retinal surface is more curve and bumpy with more intention for deformation which makes the distance measurements more sensitive to the movement of the needle tip. In conclusion, our approach can cope with the ideal 25 μm error tolerance as the average thickness of the retina is around 250 μm.

B. Primary Experiment of Injection Depth Tracking

The iRAM!S eye surgical robot with 5 DoF is utilized to perform the primary injection experiments (see Fig. 8 for experimental setup). Piezo motors (SmarACT GmbH) provide 1 μm accuracy by using PID controller with integrated incremental optical encoders. The robot is adjusted
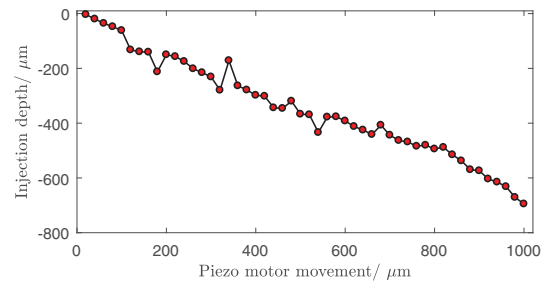

Fig. 10. The needle insertion tracking using iRM!S surgical robot on the ex-vivo porcine eyes.

manually by the adjustment bracket to make the needle tip approach to the retina. During the injection, only the motor that is holding the syringe is enabled to control the needle positioning. At the beginning we captured five cubes for needle reconstruction and calibration. Thereafter, the motor is programmed to move exact 20 μm for each step and the OCT cube is captured after each movement. Fig. 10 shows the typical tracking for the distance of needle tip to retinal surface. From this image it can be observed that there is an approximately liner increase between motor movement and insertion depth. The interaction of the needle and retinal tissue is very complicated that makes stochastic deformation of the retina. The fluctuation of the insertion depth during tracking may be as a result of distance measurement error and retina deformation.

Fig. 11 shows a few sequences of the insertion progress. The reconstruction results appropriately match with the needle tip status in en face image from the microscope. In the microscopic image, the needle tip position is significantly hard to estimate, while with our proposed method the needle tip is visualized and also the tip position and injection depth can be precisely calculated.

VI. CONCLUSION

This paper presents our novel approach to localize the needle tip inside the retina for the first time using OCT images. The presented evaluations show high accuracy distance measurement of the needle tip to retina which has mean error of 4.7 μm (maximum error 16.5 μm) for both tissue phantom and ex-vivo porcine eyes. The experiments further show the feasibility of our approach for precise needle tip localization with OCT images, given the ideal 25 μm error tolerance for subretinal injection. Our future work will focus on a injection path planning and trajectory design in a way that the drug can be delivered directly and precisely to pre-operatively defined subretinal target area avoiding critical obstacles like retinal vessels and RPE layer.

REFERENCES

[1] T. Nakano, N. Sugita, T. Ueta, Y. Tamaki, and M. Mitsuishi, "A parallel robot to assist vitreoretinal surgery," *Int. J. Comput. Assist. Radiol. Surg.*, vol. 4, no. 6, pp. 517–526, 2009.

[2] W. T. Ang, C. N. Riviere, and P. K. Khosla, "Design and implementation of active error canceling in hand-held microsurgical instrument," in *ntelligent Robot. Syst. 2001IEEE/RSJ Int. Conf.*, vol. 2. IEEE, 2001, pp. 1106–1111.
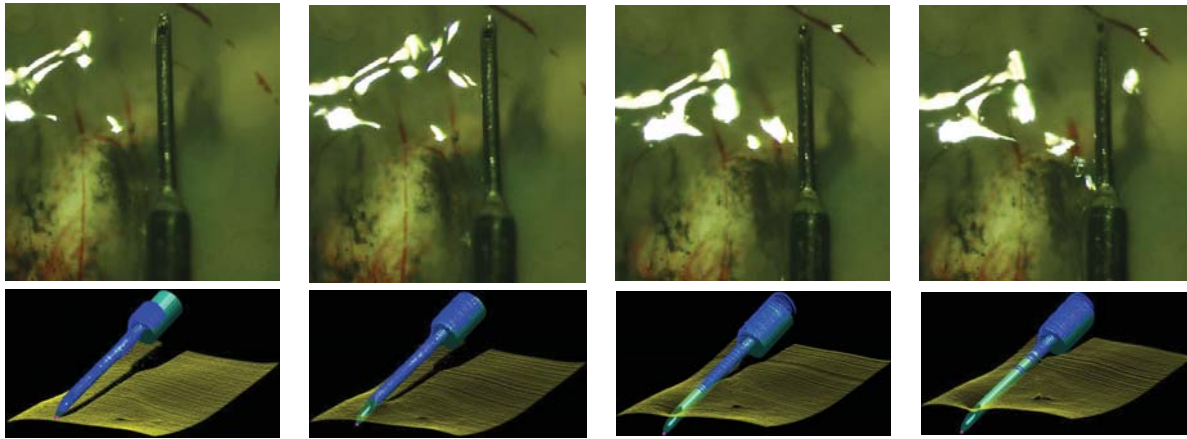
Fig. 11. The needle insertion using iRAM!S surgical robot on the ex-vivo porcine eyes.

[3] W. Wei, R. Goldman, N. Simaan, H. Fine, and S. Chang, "Design and theoretical evaluation of micro-surgical manipulators for orbital manipulation and intraocular dexterity," in *Robot. Autom. 2007 IEEE Int. Conf.* IEEE, 2007, pp. 3389–3395.

[4] R. Taylor, P. Jensen, L. Whitcomb, A. Barnes, R. Kumar, D. Stoianovici, P. Gupta, Z. Wang, E. Dejuan, and L. Kavoussi, "A steady-hand robotic system for microsurgical augmentation," *Int. J. Rob. Res.*, vol. 18, no. 12, pp. 1201–1210, 1999.

[5] F. Ullrich, C. Bergeles, J. Pokki, O. Ergeneman, S. Erni, G. Chatzipiridis, S. Pané, C. Framme, and B. J. Nelson, "Mobility experiments with microrobots for minimally invasive intraocular SurgeryMicrorobot experiments for intraocular surgery," *Invest. Ophthalmol. Vis. Sci.*, vol. 54, no. 4, pp. 2853–2863, 2013.

[6] H. C. M. Meenink, R. Rosielle, M. Steinbuch, H. Nijmeijer, and M. C. De Smet, "A master-μslave robot for vitreo-retinal eye surgery," in *Euspen Int. Conf.*, 2010, pp. 3–6.

[7] E. Rahimy, J. Wilson, T. C. Tsao, S. Schwartz, and J. P. Hubschman, "Robot-assisted intraocular surgery: development of the IRISS and feasibility studies in an animal model," *Eye*, vol. 27, no. 8, pp. 972–978, 2013.

[8] C. Song, P. L. Gehlbach, and J. U. Kang, "Active tremor cancellation by a smart handheld vitreoretinal microsurgical tool using swept source optical coherence tomography," *Opt. Express*, vol. 20, no. 21, pp. 23 414–23 421, 2012.

[9] M. A. Nasseri, M. Eder, S. Nair, E. C. Dean, M. Maier, D. Zapp, C. P. Lohmann, and A. Knoll, "The introduction of a new robot for assistance in ophthalmic surgery," in *Eng. Med. Biol. Soc. (EMBC), 2013 35th Annu. Int. Conf. IEEE.* IEEE, 2013, pp. 5682–5685.

[10] A. Gijbels, E. Vander Poorten, B. Gorissen, A. Devreker, P. Stalmans, and D. Reynaerts, "Experimental validation of a robotic comanipulation and telemanipulation system for retinal surgery," in *2014 5th IEEE RAS EMBS Int. Conf. Biomed. Robot. Biomechatronics.* IEEE, 2014, pp. 144–150.

[11] T. Meenink, G. Naus, M. de Smet, M. Beelen, and M. Steinbuch, "Robot assistance for micrometer precision in vitreoretinal surgery," *Investig. Ophthalmol. & Vis. Sci.*, vol. 54, no. 15, p. 5808, 2013.

[12] B. Gonenc, A. Chamani, J. Handa, P. Gehlbach, R. H. Taylor, and I. Iordachita, "3-DOF Force-Sensing Motorized Micro-Forceps for Robot-Assisted Vitreoretinal Surgery," *Sensors*, vol. 17, no. 11, pp. 3526–3541, 2017.

[13] N. Rieke, D. Joseph, C. Amat, F. Tombari, M. Alsheakhali, V. Belagiannis, A. Eslami, and N. Navab, "Real-time localization of articulated surgical instruments in retinal microsurgery," vol. 34, pp. 82–100, 2016.

[14] M. Waine, C. Rossa, R. Sloboda, N. Usmani, and M. Tavakoli, "3d shape visualization of curved needles in tissue from 2d ultrasound images using ransac," in *Robot. Autom. 2015 IEEE Int. Conf.* IEEE, 2015, pp. 4723–4728.

[15] Y.-J. Jo, D.-W. Heo, Y.-I. Shin, and J.-Y. Kim, "Diurnal variation of retina thickness measured with time domain and spectral domain optical coherence tomography in healthy subjects," *Investig. Ophthalmol. & Vis. Sci.*, vol. 52, no. 9, pp. 6497–6500, 2011.

[16] J. P. Ehlers, P. K. Kaiser, and S. K. Srivastava, "Intraoperative optical coherence tomography using the RESCAN 700: preliminary results from the DISCOVER study," *Br. J. Ophthalmol.*, pp. bjophthalmol–-2014, 2014.

[17] G.-W. Cheon, Y. Huang, and J. U. Kang, "Active depth-locking handheld micro-injector based on common-path swept source optical coherence tomography," in *SPIE BiOS.* International Society for Optics and Photonics, 2015, pp. 93 170U—-93 170U.

[18] H. Roodaki, K. Filippatos, A. Eslami, and N. Navab, "Introducing Augmented Reality to Optical Coherence Tomography in Ophthalmic Microsurgery," in *Mix. Augment. Reality, 2015 IEEE Int. Symp.* IEEE, 2015, pp. 1–6.

[19] B. Gonenc, R. H. Taylor, I. Iordachita, P. Gehlbach, and J. Handa, "Force-sensing microneedle for assisted retinal vein cannulation," in *IEEE Sensors Journal.* IEEE, 2014, pp. 698–701.

[20] T. T. Lam, P. Miller, S. Howard, and T. M. Nork, "Validation of a Rabbit Model of Choroidal Neovascularization Induced by a Subretinal Injection of FGF-LPS," *Investig. Ophthalmol. & Vis. Sci.*, vol. 55, no. 13, p. 1204, 2014.

[21] H. Yu, J.-H. Shen, K. M. Joos, and N. Simaan, "Design, calibration and preliminary testing of a robotic telemanipulator for OCT guided retinal surgery," in *Robot. Autom. 2013 IEEE Int. Conf.* IEEE, 2013, pp. 225–231.

[22] X. Liu, M. Balicki, R. H. Taylor, and J. U. Kang, "Towards automatic calibration of Fourier-Domain OCT for robot-assisted vitreoretinal surgery," *Opt. Express*, vol. 18, no. 23, pp. 24 331–24 343, 2010.

[23] H. Roodaki, C. A. di San Filippo, D. Zapp, N. Navab, and A. Eslami, "A Surgical Guidance System for Big-Bubble Deep Anterior Lamellar Keratoplasty," in *Int. Conf. Med. Image Comput. Comput. Interv.* Springer, 2016, pp. 378–385.

[24] M. Zhou, K. Huang, A. Eslami, D. Zapp, H. Lin, M. Maier, C. P. Lohmann, A. Knoll, and M. A. Nasseri, "Beveled needle position and pose estimation based on optical coherence tomography in ophthalmic microsurgery," in *2017 IEEE International Conference on Robotics and Biomimetics*, December 2017.

[25] M. Zhou, H. Roodaki, A. Eslami, G. Chen, K. Huang, M. Maier, C. P. Lohmann, A. Knoll, and M. A. Nasseri, "Needle segmentation in volumetric optical coherence tomography images for ophthalmic microsurgery," *Applied Sciences*, vol. 7, no. 8, p. 748, 2017.

[26] R. B. Rusu and S. Cousins, "3d is here: Point cloud library (pcl)," in *Robot. Autom. 2011 IEEE Int. Conf.* IEEE, 2011, pp. 1–4.

[27] R. B. Rusu, N. Blodow, Z. Marton, A. Soos, and M. Beetz, "Towards 3D object maps for autonomous household robots," in *Intell. Robot. Syst. 2007 IEEE/RSJ Int. Conf.* IEEE, 2007, pp. 3191–3198.

[28] H. Hoppe, T. DeRose, T. Duchamp, J. McDonald, and W. Stuetzle, *Surface reconstruction from unorganized points.* ACM, 1992, vol. 26, no. 2.

[29] L. Custodio, T. Etiene, S. Pesco, and C. Silva, "Practical considerations on Marching Cubes 33 topological correctness," *Comput. & Graph.*, vol. 37, no. 7, pp. 840–850, 2013.